Fracture Mechanics of Concrete and Concrete Structures -
High Performance, Fiber Reinforced Concrete, Special Loadings and Structural Applications- B. H. Oh, et al. (eds)

Modeling of UHPFRC I-beam with linear complementarity problem

Y. H. Guo
Harbin Engineering University, China
S.M. Han
Kumoh National Institute Technology, Gumi, Korea

ABSTRACT: This paper presents the modeling of UHPFRC I-beam with LCP. Based on the existing numerical simulation of quasi-brittle fracture in normal concrete, a model is developed to simulate the fracture in UHPFRC I-beam. A triangular unit that is constructed from constant strain triangle, with nodes along its sides and not at the vertex or the center of the unit, is used to formulate the finite element. Fracture is simulated through a hardening-softening fracture constitutive law in tension, a softening fracture constitutive law in shear and a softening fracture constitutive law in compression at the boundary nodes, with the material within the triangular unit remaining linear elastic. LCP is used to formulate the path-dependent hardening/softening behavior in non-holonomic rate form and the PATH solver is employed to solve LCP. The simulation results are in agreement with the test results, which indicate the effectivity of this method.

1 INTRODUCTION

Ultra high performance fiber reinforced concrete(UHPFRC), a relative new structure material, possesses very low permeability, extremely high compressive strength and tensile hardening because it has higher quantity of fiber reinforcement(usually 2% in volume of metallic fibers) and a denser and finer matrix. Normally the compressive strength of UHPFRC is in the range between 100 and 220 MPa, and the tensile strength of UHPFRC in the range of 7 to 15MPa.

UHPFRC has different fracture process from normal concrete because it behaves the tensile hardening after cracking in the tensile region. The fracture process of UHPFRC shown in Figure1 includes three parts. The first part is called linear-elastic zone in which there is no macro-crack and the material is regarded as linear-elasticity and isotropy. The second part is called fracture process zone or craze in which UHPFRC exhibits hardening and softening process that is different from normal concrete because normal concrete only behaves the softening process. After the linear-elastic behavior, micro-cracks develop into macro-cracks that are visible with the naked eye(ω=50μm)(Wu 2008), and a reduction in stiffness is observed. Although macro-cracks occur, the tensile stress goes on increasing because the steel fiber has much higher strength and the fiber volume fraction is 2%. When the macro-crack saturation occurs and the crack width reaches a certain magnitude, the softening occurs. The third part is called real crack zone in which no more stresses are transferred through the localized macro-cracks, and material fails and loses the load carrying capacity. As UHPFRC behaves the tensile hardening in the fracture process, the simulation of fracture in UHPFRC is different from other concrete. Hence it is significant to research the simulation of fracture in UHPFRC.

A linear complementarity problem(LCP) that is a mathematical structure consisting of a linear equation which involves two orthogonal vectors with sign constrained components is an effective approach to simulation of fracture. Many researches on applying LCP to simulate fracture have been done. Tin-Loi(2000) investigated the simulation of quasi-brittle fracture processes with the discrete-cracking model. In his investigation, the discrete-cracking model is formulated as LCP, and the PATH solver (Dirkes & Ferris 1995) is used to seek the solutions. The algorithm, PATH solver, is remarkably efficient and reasonably robust, even for the nonlinear softening case. Although one can usually assure this from the expected physical behavior of the structure, there is still no guarantee that all solutions for the given load level have been captured. Attard and Tin-Loi (2005) presented the numerical simulation of quasi-brittle fracture in concrete. In their study, LCP is used to formulate the path-dependent softening behavior, and the piecewise failure surface is modeled with two Mohr-coulomb failure surfaces and a tension cut-off. Chaimoon(2007) developed the model proposed by Attard and Tin-Loi by including a com-

pressive cap to simulate the unreinforced masonry walls under shear and compression. These models above mentioned are fit for simulating normal concrete, high-strength concrete and masonry, but not fit for UHPFRC because they do not consider the tensile hardening. In this paper, based on the investigations(Tin-Loi & Li 2000, Attard & Tin-Loi 2005, Chaimoon 2007), a model is developed to simulate UHPFRC I-beam by including a tensile hardening.

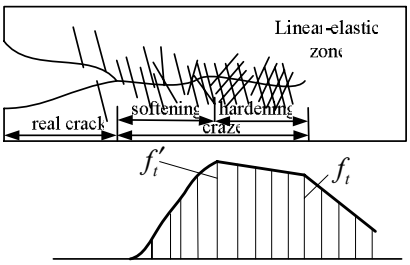

Figure 1. UHPFRC fracture process.

2 FINITE ELEMENT

The basic triangular element shown in Figure2, formed by assembling nine constant strain triangles and condensing out the freedoms at the vertices shown in Figure3(Attard & Tin-Loi 2005), is used for the fracture simulation in this model.

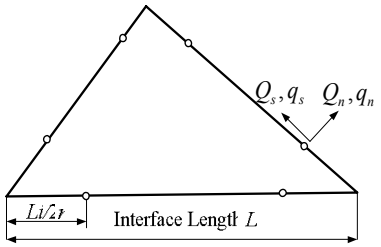

Figure 2. Basic triangular element in generalized coordinate system.

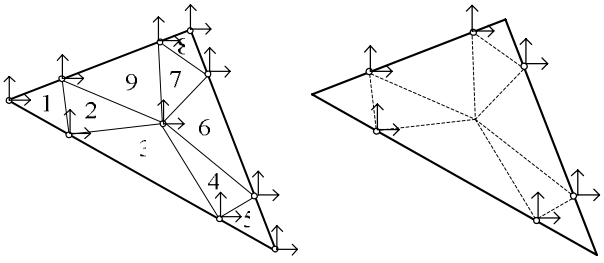

Figure 3. Form of basic triangular element (a)Uncondensed triangle (b) condensed triangle.

There are two nodes on each interface of the triangular. The interface nodes locate at $L_i/2n$ from the vertices, where L_i is the length of interface and n a choice number(n=10 in this paper). In generalized coordinate system, at each node, generalized interface displacements represented by q_i, including outward normal q_n and tangential displacement q_s, are defined. Corresponding to the generalized interface displacements at the interface nodes, the conjugate generalized forces denoted by Q_i consist of the outward normal force Q_n and the shear force Q_s.

3 CONSTITUTIVE LAW

3.1 *Inelastic yielding-failure/failure surface*

At each interface node, the piece-wise linear failure surface developed by Maier(1970) is employed to describe the inelastic yielding-failure/failure surface which is a function of normal and shear interface forces. The inelastic yielding-failure/failure surface shown in Figure4 includes two Mohr-coulomb failure surfaces, two compression caps, a tensile yielding surface and a tensile failure surface. In the investigation (Attard & Tin-Loi 2005), a tension cut-off is employed to describe the tensile failure because their investigative object is normal concrete. However it has been mentioned that UHPFRC has different tensile behavior from normal concrete and the tensile hardening must be considered in the fracture process zone. Hence the inelastic yielding-failure/failure surface in generalized force space has two surfaces employed to model the tensile behavior of UHPFRC: one is the yielding surface, and the other the failure surface. The piece-wise linear surface is named as the inelastic yielding-failure surface if it consists of the Mohr-coulomb failure surfaces, the compression caps, and the tensile yielding surface. The piece-wise linear surface is called the inelastic failure surface if it consists of the Mohr-coulomb failure surfaces, the compression caps and the tensile failure surface.

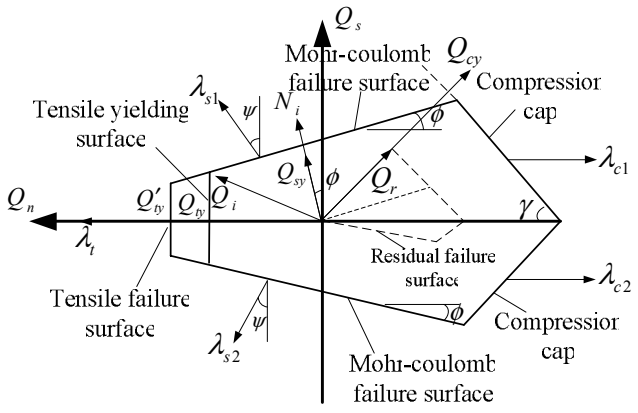

Figure 4. Interface inelastic yielding-failure/failure surface.

For the nodal interface inelastic yielding-failure/failure surfaces, the interface multipliers (λ_t, λ_{s1}, λ_{s2}, λ_{c1} and λ_{c2}) are collected in the interface multipliers vector λ_i which are irreversible deformation vector(analogous to plastic multipliers used in plasticity):

$$\lambda_i = \{\lambda_t \quad \lambda_{s1} \quad \lambda_{s2} \quad \lambda_{c1} \quad \lambda_{c2}\} \tag{1}$$

where λ_t is the multiplier associated with the tensile yielding and failure surface; λ_{s1}andλ_{s2} are the multipliers associated with the Mohr-Coulomb failure surfaces; λ_{c1} andλ_{c2} are the multipliers associated with the compression caps. In Figure4, Q_i is the resultant force vector at the interface node, Q_{ty} the tensile yielding force, Q'_{ty} the tensile failure force, Q_{sy} the shear failure force, Q_{cy} the compressive failure force and Q_r the residual compressive force. If the interface force is on the inelastic yielding-failure surface, the initial yielding-failure vector r_{i1} is defined by

$$r_{i1} = \{Q_{ty} \quad Q_{sy} \quad Q_{sy} \quad Q_{cy} \quad Q_{cy}\}^T \tag{2}$$

If the interface force is on the inelastic failure surface, the failure vector r_{i2} is given by

$$r_{i2} = \{Q'_{ty} \quad Q_{sy} \quad Q_{sy} \quad Q_{cy} \quad Q_{cy}\}^T \tag{3}$$

If the force is on the residual failure surface, the residual force vector R_i is defined by

$$R_i = \{0 \quad 0 \quad 0 \quad Q_r \quad Q_r\}^T \tag{4}$$

The interface normality matrix N_i that contains the orientations of the normal to each yielding / failure surface and the dilatancy matrix V_i that defines the flow rule for the interface irreversible deformation multipliers are respectively given by

$$N_i = \begin{bmatrix} 0 & \cos\phi & -\cos\phi & \cos\gamma & -\cos\gamma \\ 1 & \sin\phi & \sin\phi & -\sin\gamma & -\sin\gamma \end{bmatrix} \tag{5}$$

$$V_i = \begin{bmatrix} 0 & \cos\psi & -\cos\psi & 0 & 0 \\ 1 & \sin\psi & \sin\psi & -1 & -1 \end{bmatrix} \tag{6}$$

where ϕ is the friction angle, and Ψ the dilatancy angle.

The tensile yielding force Q_{ty}, the tensile failure force Q'_{ty}, the shear failure force Q_{sy}, the compressive failure force Q_{cy}, and the residual compressive force Q_r, are estimated from Equation7, Equation8, Equation9, Equation10 and Equation11, respectively.

$$Q_{ty} = \frac{f_t L_i t_i}{2} \tag{7}$$

$$Q'_{ty} = \frac{f'_t L_i t_i}{2} \tag{8}$$

$$Q_{sy} = \frac{c\cos\phi L_i t_i}{2} \tag{9}$$

$$Q_{cy} = \frac{f'_c \sin rL_i t_i}{2} \tag{10}$$

$$Q_r = \frac{f_r \sin rL_i t_i}{2} \tag{11}$$

where f_t, f'_t, c, f'_c and f_r are the tensile yielding strength, the tensile ultimate strength, the cohesion, the compressive strength and the compressive residual, respectively; t_i is the element thickness.

3.2 *Hardening/softening law*

The hardening/softening laws of UHPFRC for the interface forces at the interface nodes are shown in Figure5 in which λ^h_{tc} represents the hardening crack opening displacement and λ_{tc} the critical crack opening displacement; λ_{sc} is the critical shear displacement and λ_{cc} is the critical compressive displacement. The vertical paths represent either elastic loading or unloading. Along the hardening or softening path, the multiplier can only have positive increasing magnitude unless unloading occurs. After the critical displacement is exceeded, the crack opens or closes freely and the multiplier can increase or decrease in value.

An interface hardening/softening matrix H_i is used to represent the evolution of the inelastic yielding-failure/failure surface. If the interface forces are on the yielding-failure surface, matrix H_i is represented by H_{i1} and defined by Equation12. If the interface forces are on the failure surface, matrix H_i is represented by H_{i2} and defined by Equation13.

The off-diagonal terms in the matrix H_{i1} and H_{i2} represent interaction between the interface tensile force and the interface shear force. β is an interaction parameter. The inelastic yielding-failure/failure surface contracts in an isotropic manner if β equals to unity. It is assumed that no interaction between the shear and compression failure planes.

$$H_{i1} = \begin{bmatrix} \frac{(Q'_{ty}-Q_{ty})}{\lambda^h_{tc}} & \frac{(Q'_{ty}-Q_{ty})}{\lambda_{sc}}\beta & \frac{(Q'_{ty}-Q_{ty})}{\lambda_{sc}}\beta & 0 & 0 \\ -\frac{Q_{sy}}{\lambda^h_{tc}}\beta & -\frac{Q_{sy}}{\lambda_{sc}} & 0 & 0 & 0 \\ -\frac{Q_{sy}}{\lambda^h_{tc}}\beta & 0 & -\frac{Q_{sy}}{\lambda_{sc}} & 0 & 0 \\ 0 & 0 & 0 & -\frac{(Q_{cy}-Q_r)}{\lambda_{cc}} & 0 \\ 0 & 0 & 0 & 0 & -\frac{(Q_{cy}-Q_r)}{\lambda_{cc}} \end{bmatrix} \tag{12}$$

$$H_{i2} = \begin{bmatrix} -\frac{Q'_{ty}}{(\lambda_{tc}-\lambda^h_{tc})} & -\frac{Q'_{ty}}{\lambda_{sc}}\beta & -\frac{Q'_{ty}}{\lambda_{sc}}\beta & 0 & 0 \\ -\frac{Q_{sy}}{(\lambda_{tc}-\lambda^h_{tc})}\beta & -\frac{Q_{sy}}{\lambda_{sc}} & 0 & 0 & 0 \\ -\frac{Q_{sy}}{(\lambda_{tc}-\lambda^h_{tc})}\beta & 0 & -\frac{Q_{sy}}{\lambda_{sc}} & 0 & 0 \\ 0 & 0 & 0 & -\frac{(Q_{cy}-Q_r)}{\lambda_{cc}} & 0 \\ 0 & 0 & 0 & 0 & -\frac{(Q_{cy}-Q_r)}{\lambda_{cc}} \end{bmatrix} \tag{13}$$

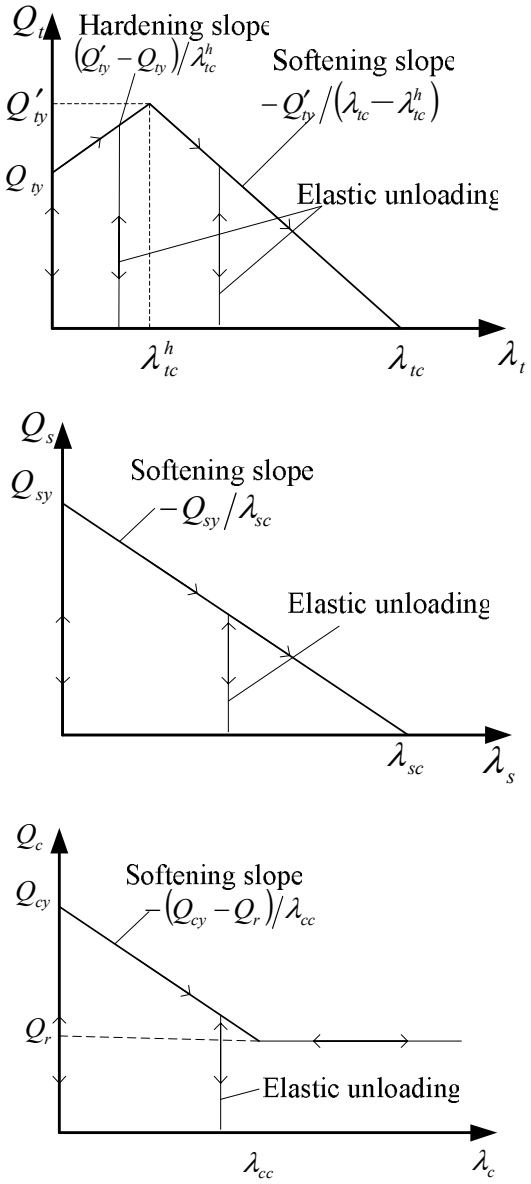

Figure 5. Interface hardening/softening law of UHPFRC for each mode(a) For tensile model (b) For shear mode (C) For compressive model.

The evolution of interface inelastic yielding-failure/failure surface is represented by the vector ξ_i

$$\xi_i = r_i + H_i \lambda_i \tag{14}$$

If the interface force is on the yielding-failure surface, r_i and H_i are respectively defined by r_{i1} and H_{i1}. The evolution of interface inelastic yielding-surface surface is presented by

$$\xi_i = r_{i1} + H_{i1} \lambda_i \tag{15}$$

If the interface force is on the failure surface, r_i and H_i are respectively defined by r_{i2} and H_{i2}. The evolution of interface inelastic failure surface is presented by

$$\xi_i = r_{i2} + H_{i2} \lambda_i \tag{16}$$

3.3 *Nonholonomic rate formulation*

For a complete structure, the interface hardening/softening matrix H_i, the interface normality matrix N_i, the interface dilatancy matrix V_i and the initial inelastic yielding-failure/failure vector r_i are collected into the structure hardening/softening matrix H, the structure normality matrix N, the structure dilatancy matrix V and the structure initial inelastic yielding-failure/failure vector r, respectively. Similarly, the generalized forces are assembled into a structure generalized force vector Q. It is noticeable that the normal interface forces at the nodes are on the yielding-failure surface or on the failure surface when assembling the structure hardening/softening matrix. At first, the structure hardening/softening matrix consists of H_{i1} because the generalized forces should firstly reach the yielding-failure surface. When the generalized force at the ith interface node reaches the failure surface, the corresponding H_{i1} of ith node should be changed into H_{i2} in the structure hardening/softening matrix H.

If the generalized force vector reaches the inelastic yielding-failure/failure surface, the inelastic yielding-failure/failure is activated. The projection of Q in all phases must satisfy the following condition.

$$0 \geq \varphi = N^T Q - r - H\lambda \tag{17}$$

Equation17 is in holonomic form and can be written in non-holonomic rate form as

$$0 \geq \dot{\varphi} = N^T \dot{Q} - H\dot{\lambda} \tag{18}$$

where φ is a potential function vector. Equation18 is a standard LCP, which satisfies the following constraints:

$$\dot{\lambda} \geq 0 \qquad \dot{\varphi}\dot{\lambda} = 0 \tag{19}$$

Equation18 can be solved by PATH solver (Dirkes & Ferris 1995) that is a mathematical program.

The above only briefly describes the form of LCP for a complete structure and the more information of the structural governing equations and the non-holonomic rate formulation can be got from Attard & Tin-Loi(2005) and Chaimmon(2007). Based on the original procedure, programs concerning the proposed constitutive law and corresponding pre- and post-processing are made. The incremental formulation of LCP in rates deriving from a non-holonomic explanation of the discontinuity displacement locus, results in the stability and bifurcation criteria and the nonconventional solution displacement. The hardening/softening behavior af-

ter linear elasticity can be effectively simulated that is the advantage of the formulation.

4 MODELING OF UHPFRC I-BEAM

4.1 *The introduction of test*

A three-point bending beam prestressed with post-tension has been tested in our lab(shown in Fig. 6). The beam with a span of 6m is simply supported on a span of 5.4m, and its section is shown in Figure7. A concentrated load was applied on the midspan. Two LVDTS were installed at the bottom midspan of the beam symmetrically. The beam was tested under the monotonic loading in an oil-pump testing machine with a capacity of 2000kN. The loading rate was 50N/s, and labview instrument was used to record the data. The failure state is shown in Figure8, in which it can be seen the main failure was the flexural cracking. The first flexural crack occurred at the bottom midspan of UHPFRC I-beam. With the load increase, multiple flexural cracks occurred near the bottom midspan.

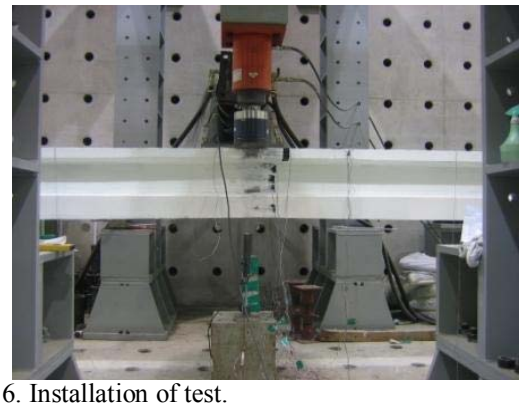

Figure 6. Installation of test.

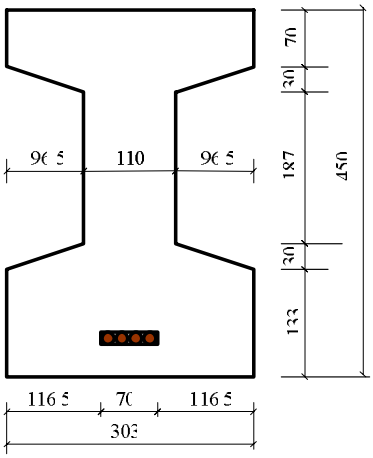

Figure 7. Section of UHPFRC I-beam.

4.2 *Numerical simulation*

The declining edges of the upper and lower flange are simplified to be straight edges shown in Figure9, in which the width and height of section that need inputting are shown. It is noted that the prestressing bar is regarded as a layer in which the UHPFRC part is ignored because this 2D model cannot consider two kinds of material properties in the same layer. The meshing of UHPFRC I-beam is shown in Figure10.

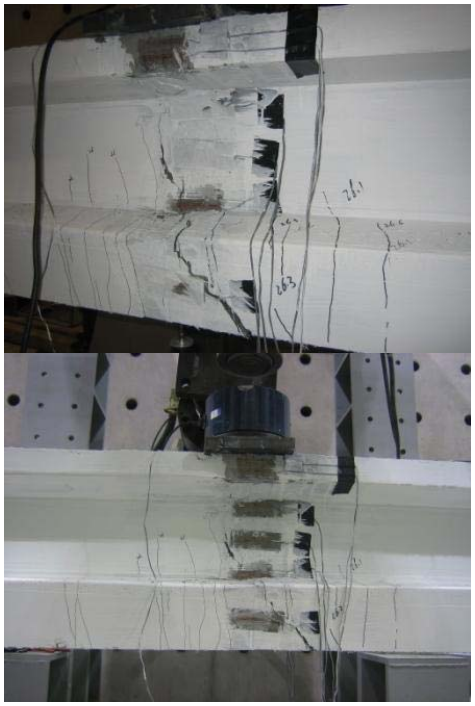

Figure 8. Failure state of UHPFRC I-beam.

For UHPFRC, Young's Modulus is 35GPa, compressive strength 140Mpa, tensile yielding strength 6MPa, tensile ultimate strength 8Mpa, friction angle and dilatancy angle 37°, hardening crack opening width 0.6mm, critical crack opening width1.5mm, critical shear opening width 1mm and critical compressive opening width 1.5mm. The magnitude of post-tensioning force is the 80% of the yielding stress. Prestressing bar is regarded as perfect plasticity, and its yielding strength and Young's modulus are 1000MPa and 186GPa, respectively. The interface nodes representing the bond slip between UHPFRC and prestressing bar have the same material parameter as UHPFRC except that the friction angle and the dilatancy angle are equal to zero.

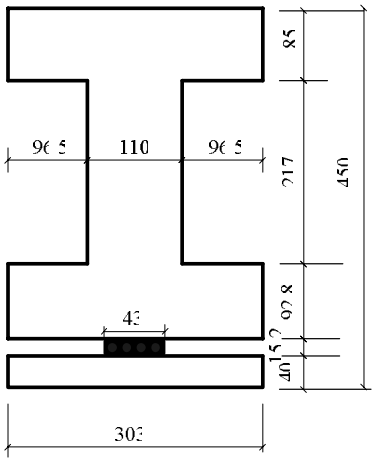

Figure 9. Simplified section.

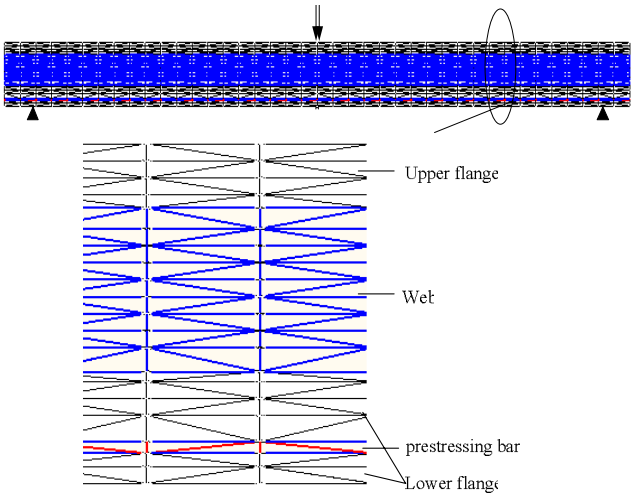

Figure 10. Meshing of UHPFRC I-beam.

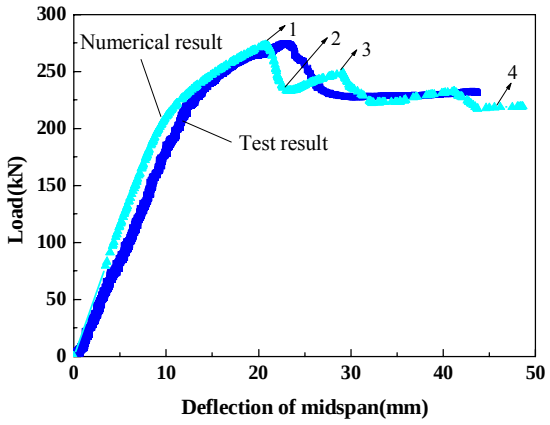

Figure 11. Load-deflection curve comparison.

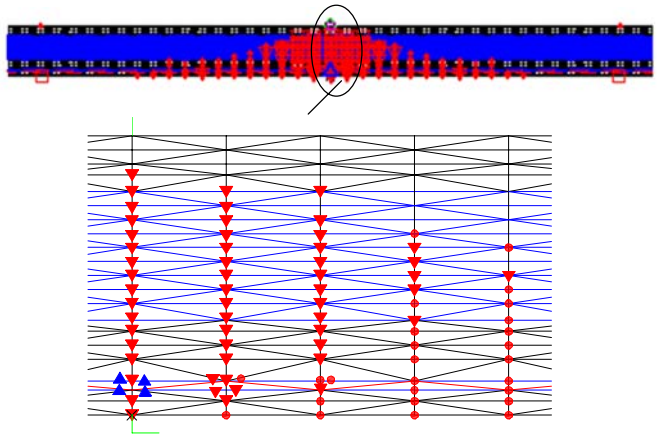

(a) Failure nodes at point 1

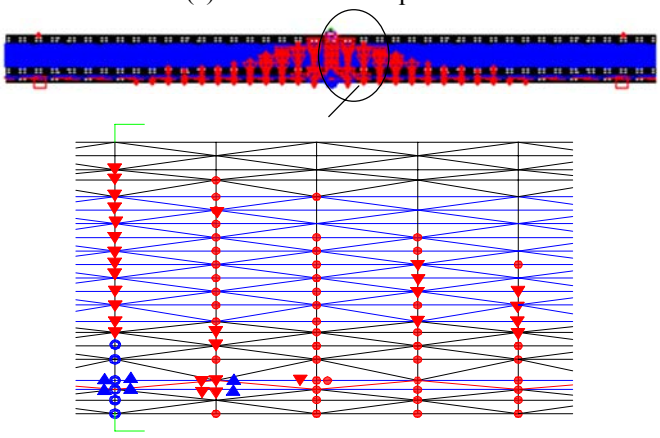

(b) Failure nodes at point 2

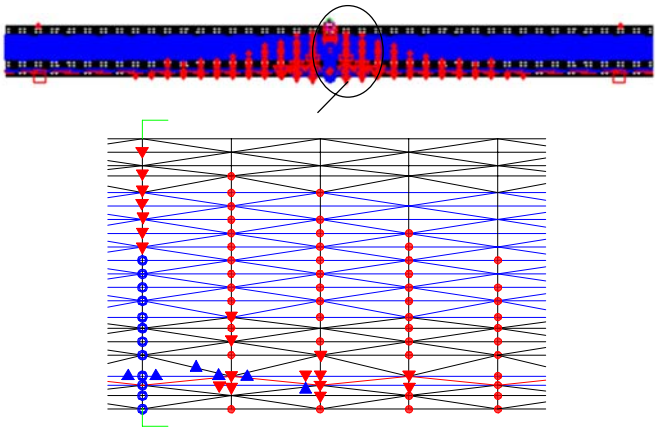

(c) Failure nodes at point 3

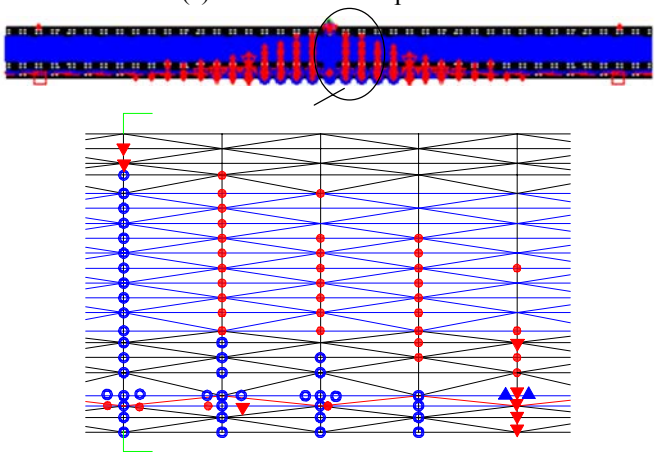

(d) Failure nodes at point 4

(○: critical displacement ▼:tensile hardening/softening ▲:shear softening *: compression softening·:Unloading)

Figure 12. Failure process after first peak load.

Table 1. Peak load and corresponding displacement comparison at the midspan.

	Peak load kN	displacement mm
Test result	274.14	23.28
Numerical result	272.89	20.75
T/N*	1.004	1.12

* T/N is the ratio of test result to numerical result

The numerical and experimental responses at the midspan are compared in Figure11, from which it can be seen that the two curves agree with each other before the peak load, and the difference is controlled within 5%. The discrepancy is relative big after peak load, which is mainly caused by the uncertainty of material inelastic properties. The numerical curve exhibits apparent unloading and reloading after the first peak load, which did not happen in the test. Although the discrepancy exists, the two responses have the similar tendency that means this model can effectively capture the beam behavior before and after peak load. The first peak load and corresponding displacement comparisons between test result and numerical result at the midspan are presented in Table1. It can be observed that both results are in good agreement with each other at the first peak load.

As shown in Figure11, this numerical simulation exists unloading and reloading after the first peak load. Hence, to be able to get a better understanding of the failure behavior of UHPFRC I-beam and how cracks propagate, several points along the load-deflection path are observed in detail. The considered points shown in Figure11 are 1, 2, 3, 4 on the load-deflection curve, and the corresponding failure nodes are shown in Figure12(a,b,c,d). In Figure12(a), unloading of some nodes occurs and no node reaches the critical crack opening displacement. The node at the bottom midspan is the first to reach the critical crack opening displacement after the first peak load, and then the tensile crack propagates from the bottom midspan to the load point that can be found in Figure12(b)(c). The tensile crack propagates sharply after the point 3, and the crack propagates not only along the section of midspan, but also both sides of midspan. Finally, the beam completely fails shown in Figure12(d). The inelastic failure during the simulation is mainly on the tensile inelastic yielding/failure surface indicating that the failure is predominately controlled by the flexural failure that is in agreement with the test result. Compared the failure state of test shown in Figure8 with that of numerical simulation shown in Figure12, it is concluded that this model simulates effectively the failure state of test.

5 PARAMETER ANALYSIS

In this paper, it is assumed that the dilatancy angle equals to friction angle, namely, an associated flow rule is adopted. Hence, the influence of different dilatancy angle on the numerical results is investigated in this section. All the parameters are the same as those above mentioned besides the different dilatancy angle. The dilatancy angle is respectively 0°, 10°, 20°, 37°.

The load-midspan deflection comparison with different dilatancy angle is shown in Figure13. As can be seen, all the curves are almost superposition before the first peak load. The curve with dilatancy angle 0° does not have the response after first peak load because all the active points unload when load reaches the first peak load. The dilatancy angle plays an important role after the first peak load, which can be seen in Figure13 that the second and third peak loads decrease with the increase of dilatancy angle. The influence of dilatancy angle on the ultimate load is shown in Figure14, from which it can be seen that the ultimate load decrease slightly with the increase of dilatancy angle.

In this study, a 37° friction angle is assumed and the associated flow rule is employed. A parametric investigation of friction angle influence is carried out here. All the parameters are the same as those above mentioned besides the different friction angle. The friction angle is respectively 30°, 37°, 40°, 45°, 50°. The associated flow rule is much fitter for the simulation that has been indicated in the investigation of different dilatancy angle. Hence the associated flow rule is also employed in the research of different friction angle.

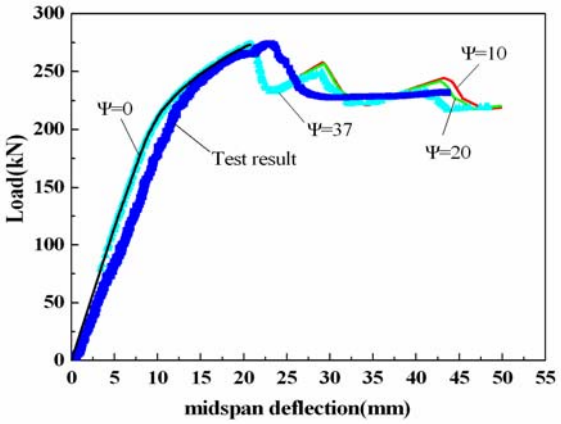

Figure 13. Load-midspan deflection comparison with different dilatancy angle.

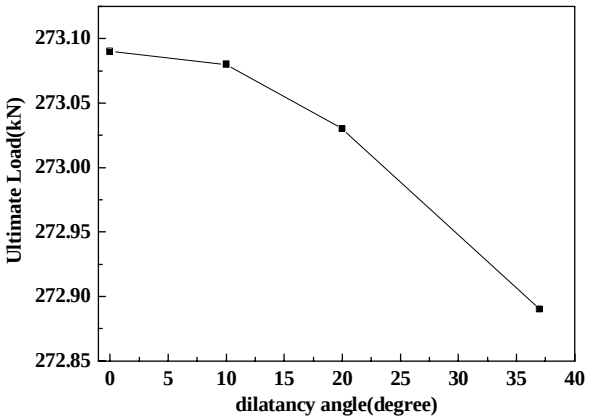

Figure 14. Relationship between the ultimate load and dilatancy angle.

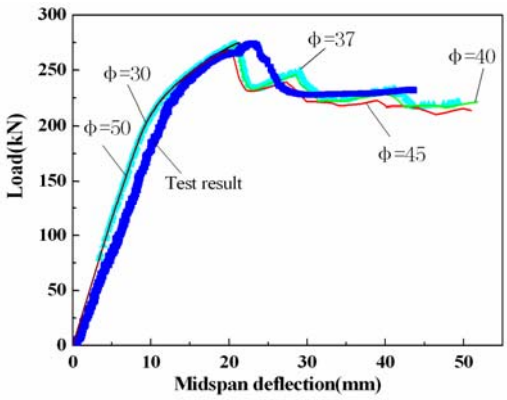

Figure 15. Load-midspan deflection comparison with different friction angle.

Figure15 shows the load-midspan deflection comparison with different friction angle, and Figure16 shows the relationship between the ultimate load and different friction angle. As can be seen, all the curves are almost superposition before the first

peak load, and with the increase of friction angle, the first peak load decreases relatively that can be clearly seen in Figure16. The curves with friction angle 30° and 50° do not have the response after first peak load, because all the active points unload when load reaches the first peak load. The friction angle also plays an important role after the first peak load, which can be seen in Figure15 that the second and third peak load decreases with the increase of friction angle.

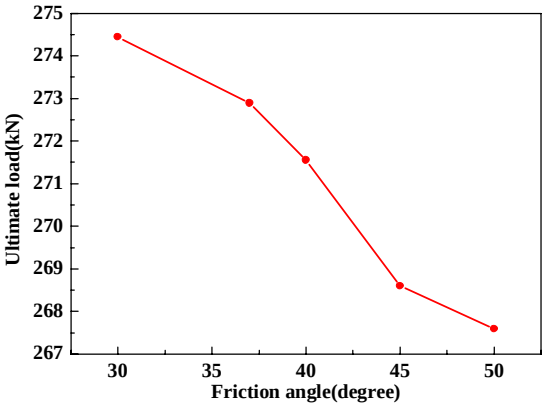

Figure 16. Relationship between the ultimate load and friction angle.

6 CONCLUSIONS

This paper deals with the modeling of fracture in UHPFRC I-beam as LCP. The inelastic yielding-failure/failure surface is modeled with two Mohr-Coulomb failure surfaces, a tension yielding surface and a tension failure surface. The fracture is simulated through a bilinear branch hardening and softening fracture constitutive law in tension and a single branch softening constitutive law in shear at the interface boundary nodes. The path-dependent behavior is solved with a LCP formulation in nonholonomic rate form. By investigation, the following conclusions can be made:

The tensile hardening after cracking must be considered for the simulation of fracture in UHPFRC.

LCP is an effective method to formulate the simulation of facture in UHPFRC.

Friction angle37° is reasonable in this numerical simulation, and associated flow rule is much fitter for the simulation.

7 ACKNOWLEDGEMENTS

This paper was one part of the research project “Development and Application of High Performance and Multi-Function Concrete” which has been accomplished now. The authors wish to express their gratitude and sincere appreciation to the financial support of “Center of Concrete Corea, Korea.”

REFERENCES

Attard, M. & Tin-Loi, F. 2005. Numerical simulation of quasi-brittle fracture in concrete. *Engineering Fracture Mechanic* 72:387-411.

Chaimmon, K. 2007. Numerical simulation of fracture in unreinforced masonry. *Ph.D thesis*.

Dirkes, S. P. & Ferris, M. C. 1995. The path solver: a non-monotone stablilization scheme for mixed complementarity problems. *Optim. Meht. Software*:123-156.

Maier G. 1970. A matrix structural theory of piecewise-linear elastoplsticity with interaction yield planes. *Meccanica* 5:54-66.

Tin-Loi, F. & Li, H. 2000. Numerical simulations of quasi-brittle fracture processes using the discrete cohesive crack model. *Mechanical Sciences* 42: 367-379.

Wu, X. G. 2008. Flexure and shear behavior of ultra high performance concrete post tension I shaped composite girder. *Ph.D thesis*.